

Characteristic Atmospheric Radiative Heating Rate Profiles in Arctic Clouds as Observed at Barrow, Alaska

D. D. TURNER

NOAA/OAR/ESRL Global Systems Division, Boulder, Colorado

M. D. SHUPE

Cooperative Institute for Research in Environmental Science, and NOAA/Earth System Research Laboratory, Boulder, Colorado

A. B. ZWINK

Cooperative Institute for Mesoscale Meteorological Studies, University of Oklahoma, Norman, Oklahoma

(Manuscript received 4 September 2017, in final form 21 December 2017)

ABSTRACT

A 2-yr cloud microphysical property dataset derived from ground-based remote sensors at the Atmospheric Radiation Measurement site near Barrow, Alaska, was used as input into a radiative transfer model to compute radiative heating rate (RHR) profiles in the atmosphere. Both the longwave (LW; 5–100 μm) and shortwave (SW; 0.2–5 μm) RHR profiles show significant month-to-month variability because of seasonal dependence in the vertical profiles of cloud liquid and ice water contents, with additional contributions from the seasonal dependencies of solar zenith angle, water vapor amount, and temperature. The LW and SW RHR profiles were binned to provide characteristic profiles as a function of cloud type and liquid water path (LWP). Single-layer liquid-only clouds are shown to have larger (10–30 K day^{-1}) LW radiative cooling rates at the top of the cloud layer than single-layer mixed-phase clouds; this is due primarily to differences in the vertical distribution of liquid water between the two classes. However, differences in SW RHR profiles at the top of these two classes of clouds are less than 3 K day^{-1} . The absolute value of the RHR in single-layer ice-only clouds is an order of magnitude smaller than in liquid-bearing clouds. Furthermore, for double-layer cloud systems, the phase and condensed water path of the upper cloud strongly modulate the radiative cooling both at the top and within the lower-level cloud. While sensitivity to cloud overlap and phase has been shown previously, the characteristic RHR profiles are markedly different between the different cloud classifications.

1. Introduction

It is well known that clouds have a substantial effect on the downwelling longwave (LW) and shortwave (SW) radiative fluxes that impinge upon the surface of Earth and upwelling fluxes at the top of the atmosphere. The magnitude of the cloud radiative effect, which is defined as the difference in the radiative flux observed in all-sky conditions versus what it would be under clear-sky conditions, is highly dependent upon both the macrophysical (e.g., height, fraction, number of layers, and temperature) and microphysical (e.g., phase, water content, particle size distribution, particle shape, and vertical distribution

within the cloud layer) properties of the cloud layers (Chen et al. 2000a,b; Brenguier et al. 2000; Shupe and Intrieri 2004; McFarlane et al. 2007; Ebell et al. 2011; Shupe et al. 2015). The accurate treatment of the radiative properties of clouds is essential for a wide range of applications including weather and climate modeling, studying the land–atmosphere interactions through the surface energy budget, and more.

Radiation is also an important component of diabatic heating within the atmosphere. The vertical distribution of radiative heating in the atmosphere has been shown to be important to large-scale circulation (e.g., Sohn 1999; Stephens 2005), but it also plays an important role on the cloud scale. When convective activity is high, such as in the tropics, radiation is a relatively small component of

Corresponding author: Dr. David Turner, dave.turner@noaa.gov

DOI: 10.1175/JAMC-D-17-0252.1

© 2018 American Meteorological Society. For information regarding reuse of this content and general copyright information, consult the [AMS Copyright Policy](https://www.ametsoc.org/PUBSReuseLicenses) (www.ametsoc.org/PUBSReuseLicenses).

the diabatic heating (Stephens 2005; Hantel and Baader 1978). However, in conditions where convective activity is low, such as in stratiform clouds, the importance of radiation in the diabatic heating of the atmosphere increases. Cloud-induced radiative heating changes the temperature profile in the vicinity of clouds and thus the local stability, sometimes inducing buoyancy-driven motions within the cloud layer. This radiatively induced turbulence is an important process in stratiform clouds (e.g., Wood 2012) and has been shown to be an especially critical component in the maintenance of long-lived single-layer mixed-phase clouds found in polar regions (Curry et al. 1996; Morrison et al. 2012; Solomon et al. 2017).

The radiative heating rate (RHR) in the atmosphere is determined by the change in net radiative flux F_{net} (defined as the net upwelling minus the net downwelling flux) over some layer that has a thickness Δp :

$$\text{RHR}(z) = \frac{dT(z)}{dt} = \frac{g}{C_p} \left(\frac{\Delta F_{\text{net}}}{\Delta p} \right) (z), \quad (1)$$

where T is temperature, t is time, p is pressure, g is the acceleration due to gravity, C_p is the specific heat content of air at constant pressure, and z is the vertical height coordinate. Thus, an increase in the net flux into a layer (i.e., flux convergence) will result in an increase in the temperature of the layer and vice versa. The total RHR is the sum of the LW and SW RHRs, and is often separated into the two components.

Observations of the RHR are challenging because radiometers that measure the upwelling and downwelling component of the radiative field must be flown at two different levels simultaneously and have matching fields of view (e.g., Francis et al. 1997; Valero et al. 1997; Zender et al. 1997; Asano et al. 2000) to determine a RHR profile. More typically, measurements from radiometers on the surface and satellites at the top of the atmosphere are used to derive a total atmospheric RHR (e.g., Slingo et al. 2009). However, in both cases, sampling uncertainties can result in large errors in the derived RHR values (e.g., Settle et al. 2008). A more common way to derive atmospheric RHR profiles is to compute them using a radiative transfer model from datasets that include the vertical distribution of temperature, gases, and cloud properties (e.g., Jensen et al. 2002; Mace et al. 2006; Mather et al. 2007; Johansson et al. 2015; McFarlane et al. 2016). However, the accuracy of the RHR profiles is strongly dependent upon the accuracy of the cloud properties used as input; for example, Ebell et al. (2011) demonstrated that the computed cloud radiative effect is dominated by uncertainties in the liquid water path (LWP) for water-bearing clouds.

There have been many papers (e.g., L'Ecuyer et al. 2008; Cesana et al. 2012; Haynes et al. 2013; Protat et al. 2014) that have characterized RHR profiles around the globe from the active remote sensors in orbit (e.g., the *CloudSat* radar and *CALIPSO* lidar); however, the temporal resolution of these spaceborne observing systems is relatively poor. Ground-based sensors have much higher temporal resolution at a given site and typically higher vertical resolution, and while there have been ground-based studies of the atmospheric RHR in the tropics and midlatitudes [e.g., Mather and McFarlane (2009) and Mace et al. (2006), respectively], previous studies that looked at the radiative impact of Arctic clouds focused on surface and/or top-of-the-atmosphere radiative fluxes and not on the RHR profiles. Given the propensity of long-lived liquid-bearing clouds in the Arctic (Shupe 2011) and the importance of radiation in the maintenance of these clouds (e.g., Morrison et al. 2012; Solomon et al. 2014), we derived the RHR from a dataset of cloud properties and atmospheric state above the U.S. Department of Energy Atmospheric Radiation Measurement (ARM) program's North Slope of Alaska (NSA) site in Barrow, Alaska (Stamnes et al. 1999; Verlinde et al. 2016), which is located at 71.323°N, 156.609°W. The resulting RHR and cloud property dataset was then analyzed as a function of cloud phase, number of layers, and other properties to develop insight into the characteristic RHR profiles above Barrow.

2. Methods

As input for calculating the RHR profiles, this analysis uses the 2-yr cloud property dataset derived from ARM observations at the NSA site between March 2004 and February 2006 (Shupe et al. 2015). This cloud property dataset consists of profiles of liquid and ice water contents and the effective radii of the liquid and ice hydrometeors at 1-min resolution. The cloud properties were derived using a multisensor approach (including observations from a 35-GHz cloud radar, polarization-sensitive lidar, microwave radiometer, infrared spectrometer, and radiosondes) that emphasized the careful determination of cloud phase with height and the accurate specification of LWP (Shupe et al. 2015). These cloud properties were used as input into a radiative closure study, which showed that the median bias in both the downwelling LW and SW flux for liquid-bearing clouds was less than 2 W m^{-2} (Shupe et al. 2015); achieving radiative closure at the surface provides some confidence that the cloud properties are accurate and thus can be used in RHR calculations. We restricted our analysis to this period because 1) the cloud properties in

this dataset provided better radiative closure in both LW and SW fluxes than an alternate cloud property dataset (Shupe et al. 2015), and 2) the cloud radar, which provides a critical input dataset to the cloud property retrieval algorithm, was not operating well either before (because of artifacts from the signal processor) or after (because of a failure in the waveguide) this period (Kollias et al. 2016). While this 2-yr dataset does not represent a climatology of the clouds at the NSA site, this dataset is a continuous and consistent representation of the clouds over those two years.

These cloud properties were then used as input into the radiative transfer models RRTM_LW and RRTM_SW (Mlawer et al. 1997; Iacono et al. 2008; Mlawer et al. 2016) to compute RHR profiles. Additional information is required for the RHR calculations. The atmospheric state (i.e., temperature and humidity structure) required for the radiative transfer calculations was derived from twice-daily radiosondes that were interpolated over the diurnal cycle and blended with analysis fields from the European Centre for Medium-Range Weather Forecasts operational model (Shupe et al. 2015); this model provided the atmospheric state above the maximum height of the sonde profile and was used to fill any gaps that extended more than 12 h. The 1-min resolution humidity profiles from this interpolated product were scaled with a height-independent scale factor so that they agreed with the precipitable water vapor retrieved from the collocated microwave radiometer, which was retrieved using the algorithm of Turner et al. (2007). The surface albedo, when the solar zenith angle (SZA) was less than 85° , was derived from upward- and downward-facing pyranometers at the NSA site. The skin temperature, which is needed for the LW calculations, was derived from a downward-facing pyrgeometer assuming the surface emissivity was 1. No aerosols were used in the RHR calculations. The subarctic summer (May–September) and winter (October–April) atmospheres provided the concentrations of important radiatively active trace gases (McClatchey et al. 1970). We subsampled the 1-min cloud property dataset, computing RHR profiles every 10 min. Note that the RRTM models were run twice for each sample in our dataset; once with the cloud properties included, and once with the clouds removed thereby providing a cloud-free RHR calculation.

Our analysis will characterize the RHR as a function of the properties of the cloud(s) above the NSA site. We will use the number of cloud layers as one component of our analysis; cloud layers are considered independent if separated by at least two hydrometeor-free cloud radar bins (90 m). To ensure robust statistics and minimize the impact of transient amounts of cloud liquid or ice, we will assume liquid exists in a layer if the LWP for that cloud layer is greater than 1 g m^{-2} , and that ice exists in

that layer if the ice water path (IWP) in that layer is greater than 10 mg m^{-2} . (Our results are relatively insensitive to these thresholds.) The thickness of the cloud layer was computed differently for ice-only clouds versus clouds that contained liquid water. If the cloud was ice only, then the thickness is the distance from the lowermost to uppermost radar bin with ice hydrometeors in the contiguous layer. If the cloud was liquid-bearing, then the thickness was computed as the distance between the lowermost and uppermost bins that contained liquid water. As an example, the thickness of a mixed-phase cloud that is composed of a liquid-topped cloud layer with ice precipitating from the bottom (which is a cloud type commonly observed in the Arctic) is the thickness of the liquid layer.

We will consider the LW and SW RHR profiles separately in our analysis. All of the available data will be used to derive the characteristic LW RHR profiles for the different cloud classifications. However, we will limit our analysis of the SW RHR to cases where the SZA is less than 75° ; this reduces complications associated with very low solar elevation conditions. However, by restricting the SW analysis to those cases when the sun is high, the number of samples is greatly diminished, and thus makes it more challenging to draw statistically definitive results when we further subset the data (e.g., by surface albedo and LWP). These limitations will be discussed in more detail below.

3. Results

a. Seasonal cycle

There is a strong annual cycle to the distribution of liquid and ice hydrometeors above Barrow. The two years of observations and all-sky model calculations from these 10-min resolution observations were composited into monthly mean profiles to show this annual cycle (Fig. 1). The distribution of mean all-sky liquid water content (LWC; Fig. 1c) shows that the liquid water is distributed higher in the troposphere during the summer and early autumn, with significant average amounts of LWC (0.1 g m^{-3}) existing at 6 km or higher. During these months, we also note that the largest mean LWC ($\sim 1 \text{ g m}^{-3}$) occurs in the lowest 500 m throughout the summer, but this layer of high mean LWC becomes significantly deeper and reaches ~ 1.5 -km depth in September, October, and into early November. The late winter–early spring has the smallest mean LWC values, but there are times when the mean LWC value reaches 0.1 g m^{-3} at low levels. The mean all-sky ice water content (IWC; Fig. 1d) also shows a strong seasonal cycle, with the lowest values (0.05 g m^{-3}) in the January, February, and early March. The mean value of IWC in the lowest 2 km

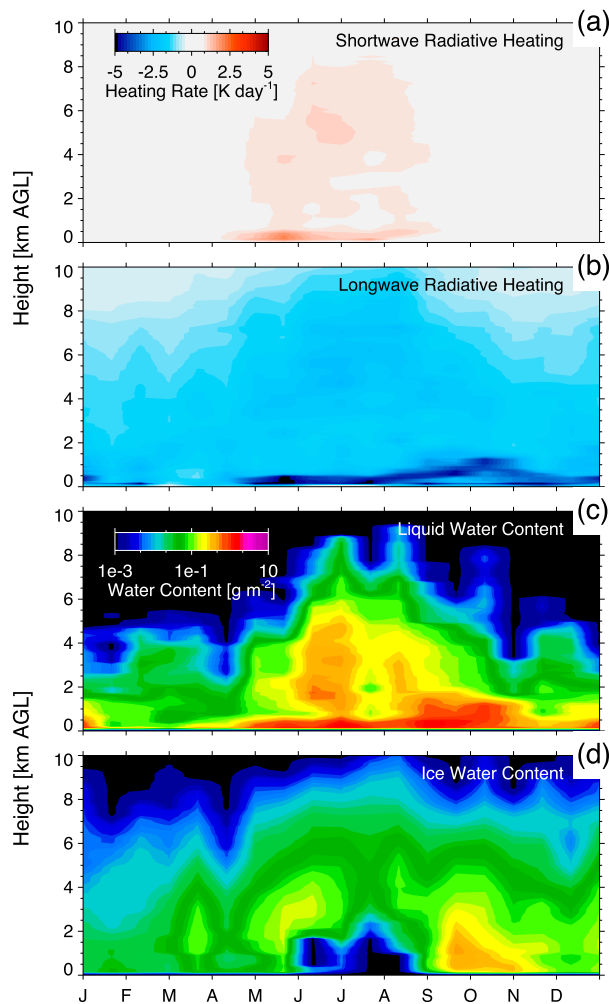


FIG. 1. A composite showing the yearly evolution of the monthly mean all-sky RHR profiles due to (a) SW and (b) LW radiation, as well as the evolution of the vertical distribution of monthly mean (c) LWC and (d) IWC.

during the summer months is very small because of the warmth of the atmosphere; the low-level clouds during this period are composed primarily of liquid hydrometeors. The highest mean IWC values, with values approaching 0.3 g m^{-3} , are found in the lowest 2 km during the autumn. These all-sky LWC and IWC results are the product of the cloudy-sky water contents and cloud occurrences for liquid and ice, respectively, given in Fig. 4 of Shupe et al. (2015). The reader is referred to Shupe et al. (2015) for more details on cloud occurrence statistics. Here, all-sky values are considered to enable comparison with all-sky RHRs.

This seasonal cycle of cloud properties imparts a strong seasonal cycle on the mean all-sky RHR profiles. The vertical distribution of the hydrometeors, and primarily the liquid water, results in SW radiative heating (Fig. 1a) from the surface to nearly 8 km from May

through late August, with the strongest mean SW radiative heating occurring in the lowest 500 m in May corresponding to a period when there are large mean LWC values in the lowest 500 m and relatively lower mean LWC and IWC values above it. The effect of the clouds on the LW RHR, in a mean sense, is to cool the atmosphere (Fig. 1b) with the strongest mean LW radiative cooling associated with the low-level liquid clouds where the mean LWC values are approximately 1.0 g m^{-3} .

b. Basic characterization and data selection

To understand the effect of clouds on the radiative heating of the atmosphere, we simplified the analysis by segmenting the results as a function of cloud type. There were 95 430 samples in our 2-yr dataset. During this 2-yr period, the sky was cloud free directly above the ARM NSA site approximately 27% of the time, had single-layer clouds 44% of the time and double-layer clouds 22% of the time, and the remaining 7% of the cases had 3 or more cloud layers. Note that the monthly distribution of cloud phase is shown in Shupe et al. (2015) and thus is not replicated here. Our analysis here will primarily focus on single-layer clouds, of which 45% were liquid only, 24% were ice only, and the remaining 31% were mixed phase (i.e., contain both ice and liquid hydrometeors in a single contiguous cloud layer).

Our goal is to investigate the characteristic RHR profiles of clouds from these three types. Thus, we decided to only include clouds in our analysis where the lowest level of the cloud was at least 200 m above the ground, so that we could investigate the impact the cloud has on the radiative heating rate profile below the cloud. For the typical mixed-phase cloud that is topped with liquid water, this implies that the liquid layer be at least 200 m above the ground; the precipitating ice could extend to the surface. Furthermore, we required the cloud layer have a minimum vertical extent of at least three continuous radar bins (i.e., 135 m) to be included in the analysis. Last, as we wanted to look at clouds as a function of LWP, and less than 5% of liquid-bearing clouds had a LWP greater than 300 g m^{-2} (Fig. 2a), we limited our analysis of liquid-bearing clouds to those with LWP below this threshold. These restrictions reduced the number of single-layer clouds, resulting in 2782 liquid-only, 6462 mixed-phase, and 6056 ice-only clouds.

c. Mixed-phase versus single-phase cloud distributions

Two clouds that have the same total condensed water path can have markedly different effects on the radiative fields (e.g., Key and Intrieri 2000; Cesana and Storelmo 2017), and thus we start our analysis by looking at the properties of the clouds in our dataset. A natural question is this: How do the physical properties of single-layer

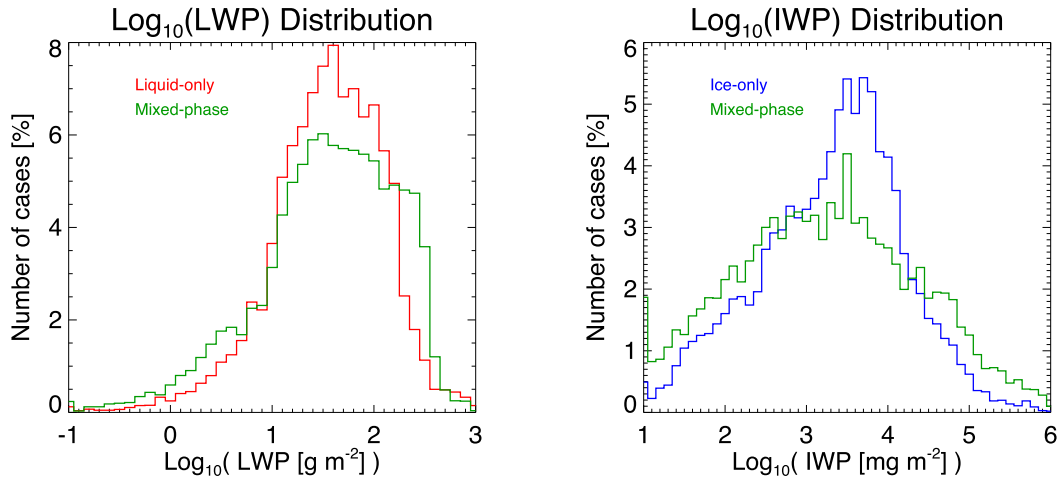


FIG. 2. The distribution of the logarithm of (left) LWP and (right) IWP in single-layer liquid-only (red), ice-only (blue), and mixed-phase (green) clouds over the 2-yr dataset.

mixed-phase clouds differ from their single-phase cousins? First, the distributions of LWP and IWP are markedly different. The LWP distribution for single-layer cases examined here (Fig. 2a) shows that for clouds with LWP values between 10 and 120 g m⁻² there are more liquid-only than mixed-phase clouds, but the opposite is true for LWP values less than 10 or greater than 120 g m⁻². The IWP distribution (Fig. 2b) shows a similar feature, where clouds with IWP values between 1 and 12 g m⁻² are more frequently ice only than mixed phase.

A second difference between mixed-phase and single-phase single-layer clouds is their distribution of geometric cloud thickness (Fig. 3). The liquid-only cloud thickness distribution could be represented by a gamma distribution with a peak in the distribution of approximately 160 m. The mixed-phase cloud distribution

appears to be bimodal, with peaks at 180 and 400 m; however, it is possible that this is due to sampling and that a larger dataset might show that the distribution is really single modal. The ice-only cloud thickness has the broadest distribution, with values ranging from several hundred m to over 6 km.

There is also a significant difference in the seasonal distribution of the LWP in single-layer clouds (Fig. 4). Both the liquid-only and mixed-phase clouds have a minimum LWP in March and April, and the range of both categories is smallest in April. However, the monthly median LWP for liquid-only clouds peaks in August and September, whereas for mixed-phase clouds the median LWP peaks in October (although the values for August and September are also reasonably large).

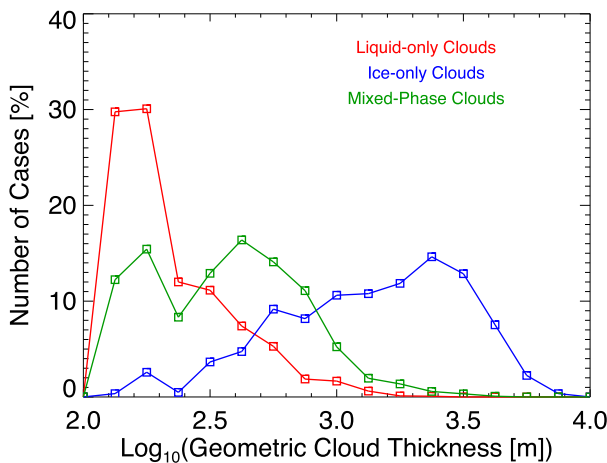


FIG. 3. The distribution of the log of the cloud thickness for single-layer liquid-only (red), ice-only (blue), and mixed-phase (green) clouds from the 2-yr dataset.

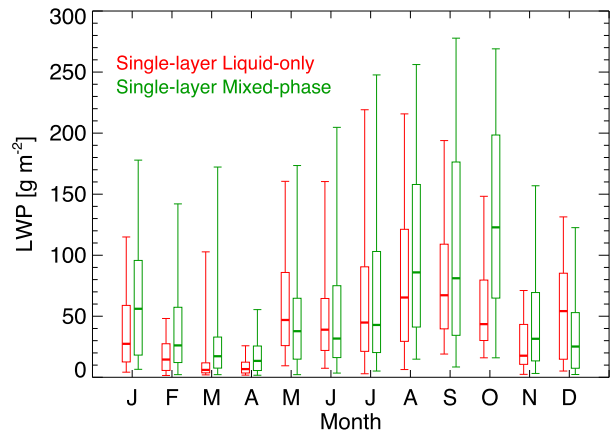


FIG. 4. The monthly distribution of LWP for single-layer liquid-only (red) and mixed-phase (green) clouds from the 2-yr dataset. The median is given by a thick horizontal line in the center of the box, the interquartile spread by the box, and the 5th and 95th percentiles by the whiskers.

For most months, the median LWP for mixed-phase clouds is larger than the median LWP for liquid-only clouds; the exceptions to this is December (where the liquid-only median LWP is markedly higher than that for mixed-phase clouds) and May, June, and July where the median LWP for liquid-only clouds is only slightly higher than that for mixed-phase clouds. However, for all months except December, the range of LWP is larger for the mixed-phase clouds, and in many months the range is considerably larger.

Interpreting the monthly distribution of IWP for mixed-phase and ice-only clouds (Fig. 5) is not as clear. The primary signal in this figure is that the range of IWP, as expressed by the spread between the 95th and 5th percentiles, is larger in all months for mixed-phase clouds than ice-only clouds. The interquartile spread is usually larger for the mixed-phase clouds also, but not for all months. Median IWP values are often similar, with mixed-phase clouds having somewhat higher values in June–August and single-phase clouds having higher medians through the rest of the year.

d. Characteristic single-layer ice-only cloud RHR profiles

As the total water path is the main modulator of the radiative field, we sorted our data into bins by the water path so that the different bins had roughly the same number of observations. We then interpolated the radiative heating rate of all single-layer clouds onto a normalized height grid to investigate the radiative heating between the cloud base and Earth's surface, between the cloud base and cloud top, and above the cloud. The normalized height grid for single-layer clouds (used in Figs. 6, 7, and 10) was defined as a linear scale from 0 to 3, where the surface was level 0, cloud-base height was level 1, cloud-top height was level 2, and 10 radar bins above cloud-top height was level 3; the RHR profiles were interpolated to this vertical grid.

Figure 6 shows the characteristic vertically normalized LW (Fig. 6, left) and SW (Fig. 6, right) RHR profiles for single-layer ice-only clouds, wherein the cases were separated into six IWP bins (Table 1). The characteristic clear-sky RHR profiles, which were computed for the same samples using the RRTM model without cloud input, are shown in Fig. 6 as the cyan lines. Note that these clear-sky profiles show slight structure in RHR relative to the normalized cloud boundaries because of enhanced water vapor at those heights. For the IWP bins with small amounts of ice, the median LW and SW RHR profiles are only slightly different than the clear-sky profiles, with a small amount of additional LW radiative cooling inside the cloud, very little SW warming inside the cloud, and no significant impact

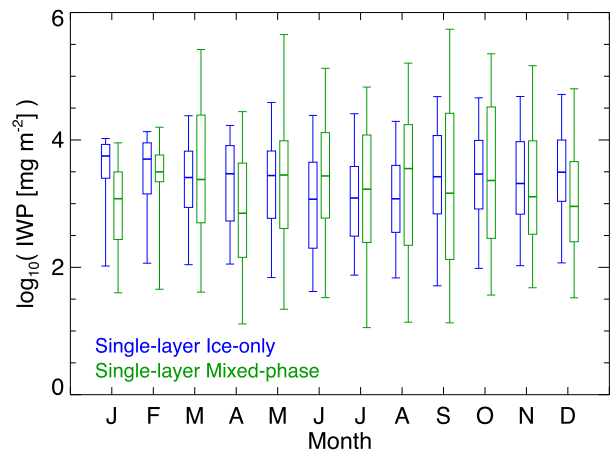


FIG. 5. The monthly distribution of the log of IWP for single-layer ice-only (blue) and mixed-phase (green) clouds from the 2-yr dataset. The median is given by a thick horizontal line in the center of the box, the interquartile spread by the box, and the 5th and 95th percentiles by the whiskers.

either above or below the cloud. However, as the IWP increases above 5 g m^{-2} (red, purple, and gray lines) there is significantly more LW radiative cooling inside the cloud with rates of $2\text{--}3 \text{ K day}^{-1}$ above the clear-sky value; this agrees very well with the 3 K day^{-1} value suggested by Curry et al. (1996). This LW cooling is partially, but not fully, offset by SW heating inside the cloud. Furthermore, for these cases, there is also some LW radiative heating (relative to the LW clear-sky RHR profile) below the cloud that diminishes with distance away from the cloud, and for the class with the highest IWP values ($30\text{--}100 \text{ g m}^{-2}$) there is even radiative heating (again relative to the clear-sky profile) in the lowest part of the cloud. This LW radiative heating (relative to clear sky) below the cloud is partially offset by slight SW radiative cooling (relative to clear sky). Note that the SW RHR profile for the highest IWP bin is not shown in Fig. 6 (right) because there were very few samples and thus the statistics were poor.

e. Characteristic single-layer liquid-bearing cloud LW RHR profiles

The same analysis was performed to determine the characteristic LW RHR for single-layer liquid-bearing clouds (i.e., liquid only and mixed phase). The median RHR profile was computed for all clouds that have LWP in five separate bins: 1–10, 10–30, 30–60, 60–120, and $120\text{--}300 \text{ g m}^{-2}$. These bins were chosen such that the number of cases in each bin is roughly equivalent (Table 2). There are approximately 2–3 times as many mixed-phase cloud events in each LWP bin than liquid-only cloud events.

The median LW RHR profiles for liquid-only clouds are shown in Fig. 7a. The bin with the lowest LWP shows

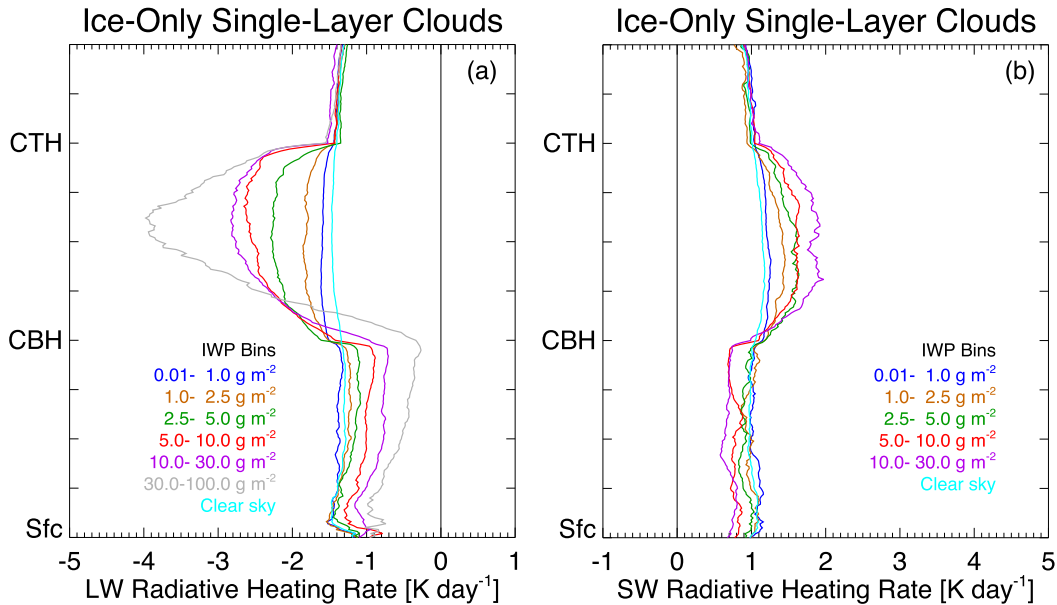


FIG. 6. The normalized vertical distribution of the median (left) LW RHR and (right) SW RHR for single-layer ice-only clouds using the IWP specified in Table 1 between the surface (Sfc), cloud base (CBH), and cloud top (CTH). The median clear-sky RHR profiles are also shown. The number of cases in each bin is given in Table 1. Because of the small number of cases, the median SW RHR result is not shown for the largest IWP bin.

relatively uniform LW radiative cooling throughout the cloud at approximately $10\text{--}15\text{ K day}^{-1}$ cooling. However, as the LWP increases, the LW radiative cooling at cloud top increases dramatically, and is focused on a narrower layer, with cooling rates at cloud top above 80 K day^{-1} for clouds with LWP in the $120\text{--}300\text{ g m}^{-2}$ range. Interestingly, this shape of the LW radiative cooling within the cloud changes noticeably as the LWP increases, with the bottom portion of the cloud having smaller LW cooling rates, and for clouds in the larger LWP bins there is even some small amount of LW radiative heating near cloud base with rates approaching 5 K day^{-1} (Fig. 7b). This vertical distribution of LW radiative effects, especially for clouds with larger LWP values, could create an unstable environment (if all other processes are held fixed), which would then result in turbulent mixing as colder parcels from the upper part of the cloud sink and warmer parcels rise. This turbulent mixing, driven largely by LW radiative flux divergence at cloud top, is hypothesized to play a significant role in the maintenance of liquid-bearing clouds in the Arctic (Morrison et al. 2012).

The same analysis was performed for single-layer mixed-phase clouds (Fig. 7c). Qualitatively, the characteristic LW RHR profiles for mixed-phase clouds are similar to liquid-only clouds. However, the magnitude of radiative cooling at cloud top for a given LWP bin is slightly smaller for mixed-phase clouds relative to liquid-only clouds; this is true for the radiative cooling throughout the cloud.

The differences between the vertically normalized LW RHR profiles between liquid-only and mixed-phase clouds for each LWP bin are shown in Fig. 7d. The difference in the maximum cooling rate is about 30 K day^{-1} for clouds with LWPs in the $120\text{--}300\text{ g m}^{-2}$ bin, which occurs not at cloud top but at an altitude slightly below cloud top, indicating differences in the shapes of the profiles of LWC and IWC, and thus RHR, in the cloud. The differences in RHR profiles for cases with moderate LWP between 10 and 120 g m^{-2} are relatively similar.

We believe that the difference in the median RHR profile (for a given LWP range bin) between liquid-only and mixed-phase clouds is primarily related to the vertical distribution of the LWC within the clouds. The median LWC and thickness for the liquid-only and mixed-phase single-layer clouds are provided in Table 3. The median LWC in mixed-phase clouds is about 60% of the LWC in single-layer liquid-only clouds; however, to keep the LWP about the same the mixed-phase clouds are thicker (i.e., have more vertical extent) than the liquid-only clouds by 25%–50%. By distributing the liquid water over a larger vertical distance, the vertical profile of cloud optical depth has smaller magnitudes in mixed-phase clouds than liquid-only clouds, which affects the radiative divergence and thus the RHR profile. Yet, the fact that the mixed-phase clouds are thicker results in a relative vertical compression of the strongest cooling near cloud top when viewed in the vertically normalized perspective. Furthermore, the addition of

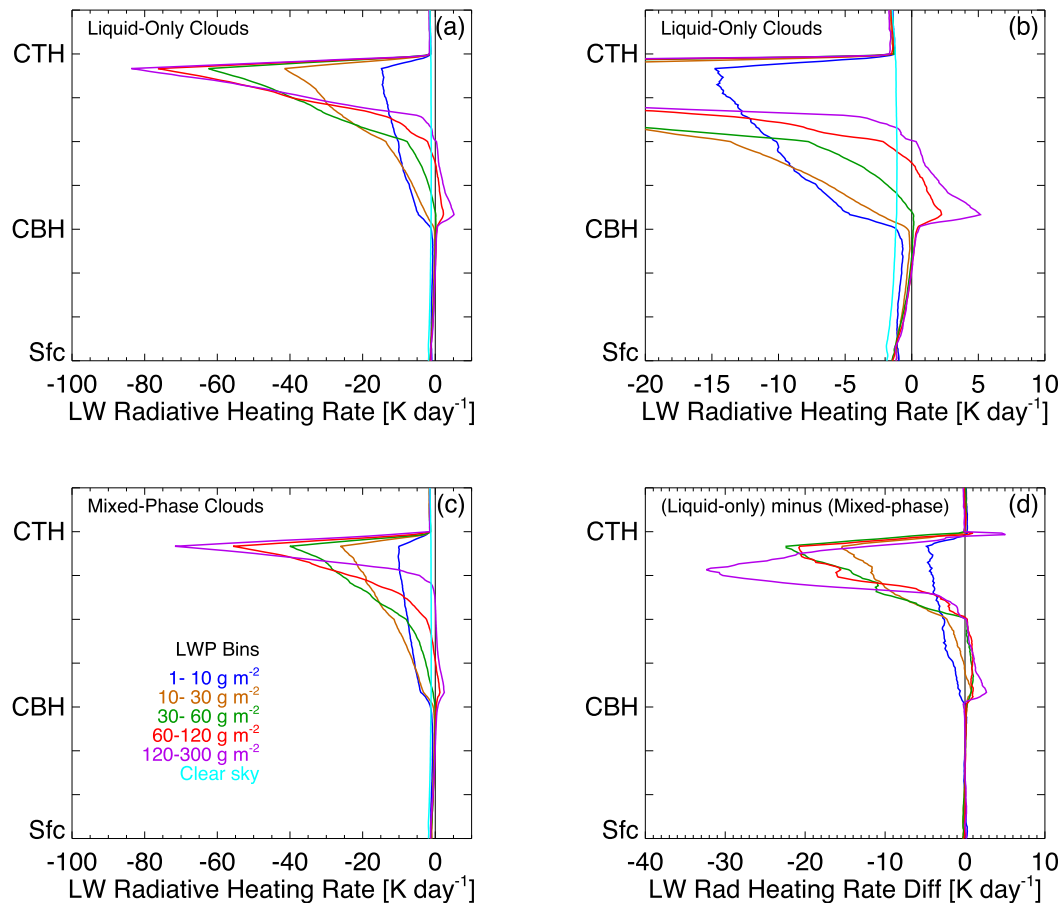


FIG. 7. The normalized vertical distribution of the median LW RHR for single-layer liquid-bearing clouds using the LWP bins specified in Table 2 between Sfc, CBH, and CTH. The median clear-sky LW RHR profiles are also shown. (a) Median profiles for liquid-only clouds, (b) median profiles for liquid-only clouds focusing on the values on the lower part of the profile (zoomed x axis), (c) median profiles for mixed-phase clouds, and (d) differences between the median profiles of liquid-only and mixed-phase clouds.

the IWC in the bottom of the liquid layer of mixed-phase clouds increases the cloud optical depth in the lower part of the cloud somewhat, further affecting the radiative divergence at the bottom of the mixed-phase cloud. Last, it is noteworthy that the ice falling below the liquid layer in mixed-phase clouds has relatively little impact on the RHR below cloud base. Stephens (1978) showed the sensitivity of the radiative heating rate to the LWC profile, given a fixed LWP value, many decades ago.

The characteristic (i.e., median) LW RHR profiles for each LWP bin provide insight into the impact of these single-layer liquid-bearing clouds on the atmosphere within and around the cloud. However, it is also useful to look at RHR distributions at cloud top and cloud base and how they are different between liquid-only and mixed-phase clouds as a function of LWP. The distribution of the LW RHR at cloud top (i.e., at the uppermost radar bin for the cloud) for each of the LWP bins is shown in Fig. 8. The most remarkable difference is that

the distribution is shifted to larger cooling rates for liquid-only clouds relative to mixed-phase clouds for all LWP bins; this is especially true for clouds in the 30–60 and 60–120 g m^{-2} bins (Figs. 8c,d, respectively) where the shift to larger cooling rates is much larger. Interestingly, for mixed-phase clouds with LWPs less than 60 g m^{-2} (i.e., Figs. 8a–c) there is a peak in the LW

TABLE 1. Number of ice-bearing single-layer clouds in each IWP bin for both the LW (all cases) and SW statistics (only when the $\text{SZA} < 75^\circ$) shown in Fig. 6.

IWP bin range (mg m^{-2})	LW no.	SW no.
10–1000	2079	609
1000–2500	984	258
2500–5000	949	207
5000–10 000	943	226
10 000–30 000	819	186
30 000–100 000	282	47
Total range: 10–100 000	6056	1533

TABLE 2. Number of clouds in each LWP bin for liquid-bearing clouds for all cases and for only cases for which the SZA < 75°.

LWP bin range (g m^{-2})	Liquid-only clouds (all SZAs)	Mixed-phase clouds (all SZAs)	Liquid-only clouds (SZA < 75°)	Mixed-phase clouds (SZA < 75°)
1–10	330	958	87	155
10–30	619	1387	224	265
30–60	739	1227	248	168
60–120	684	1309	304	134
120–300	410	1581	184	161
Total range: 1–300	2782	6462	1047	883

cooling rates of about 5 K day^{-1} ; this is due to a large number of cases where there is a significant amount of IWC at cloud top (i.e., above the liquid in the cloud below) that serves to partially attenuate that LW radiative cooling from the liquid portion of the clouds.

The distribution of the LW radiative heating rate at cloud base (i.e., the lowest radar bin that contains liquid water) in the single-layer liquid-bearing clouds is much different than the situation at cloud top. For clouds with LWP in the range from 1 to 10 g m^{-2} , the distribution of LW radiative heating for liquid-only clouds is shifted to slightly smaller values than mixed-phase clouds (Fig. 9a) showing that the liquid-only clouds cool the atmosphere a bit more efficiently than mixed-phase clouds; this is due primarily to the difference in the distributions of LWC within the cloud but also to the partial attenuation of the ice in the mixed-phase clouds. However, this is reversed for all clouds with LWP greater than 10 g m^{-2} wherein the liquid-only clouds have larger radiative heating rate values at cloud base than mixed-phase clouds (Figs. 9b–e). For clouds with LWP values greater than 120 g m^{-2} , both liquid-only and mixed-phase typically clouds warm the atmosphere at cloud base because of radiative flux convergence [this was also observed by Slingo et al. (1982) for midlatitude marine stratocumulus clouds], but the liquid-only clouds are more efficient at this primarily because of the higher LWC values in the liquid-only clouds.

f. Characteristic single-layer cloud SW RHR profiles

A similar analysis as above was performed to derive characteristic SW RHR profiles in single-layer liquid-only

and mixed-phase clouds as a function of LWP (the single-layer ice-only results were shown in section 3d). These results for the liquid-only and mixed-phase clouds, which only include cases when the SZA < 75°, are shown in Fig. 10. By restricting our analysis to this subset of data, the number of cases used in the SW analysis is 3–5 times smaller than the number of cases used in the LW analysis (Table 2).

The SW RHR profiles show a similar vertical structure (Fig. 10), albeit with opposite sign, as the LW RHR profiles (Figs. 7a,c) in that the largest absolute RHR values are located near cloud top, and decrease toward the cloud base. However, the magnitude of the SW heating rates is much smaller than LW cooling rates for a given LWP bin. Furthermore, the SW RHR profiles show very small differences (less than 2 K day^{-1}) between liquid-only and mixed-phase clouds, for a given LWP bin (Fig. 7d). Thus, the SW radiative heating partially offsets the LW radiative cooling. Similar to the LW RHR profiles, the SW RHR profiles show the maximum SW heating occurring over a somewhat shallower normalized height layer for mixed-phase clouds relative to liquid-only clouds.

The magnitude of the SW RHR does depend on both the SZA and the surface albedo. As the SZA decreases (i.e., the sun is higher in the sky), the effective cloud optical path decreases thereby giving less opportunity for photons from the sun to be absorbed by the cloud and thus the SW RHR decreases. Similarly, as the surface albedo increases, more solar photons are reflected upward from the surface back into the cloud, providing additional opportunities for these photons to

TABLE 3. Statistics of liquid-bearing single-layer clouds.

LWP bin range (g m^{-2})	Median LWC for liquid-only clouds (g m^{-3})	Median LWC for mixed-phase clouds (g m^{-3})	Median thickness for liquid-only clouds (m)	Median thickness for mixed-phase clouds (m)
1–10	0.030	0.023	189	200
10–30	0.079	0.053	189	252
30–60	0.184	0.111	189	315
60–120	0.298	0.190	189	378
120–300	0.541	0.320	252	567

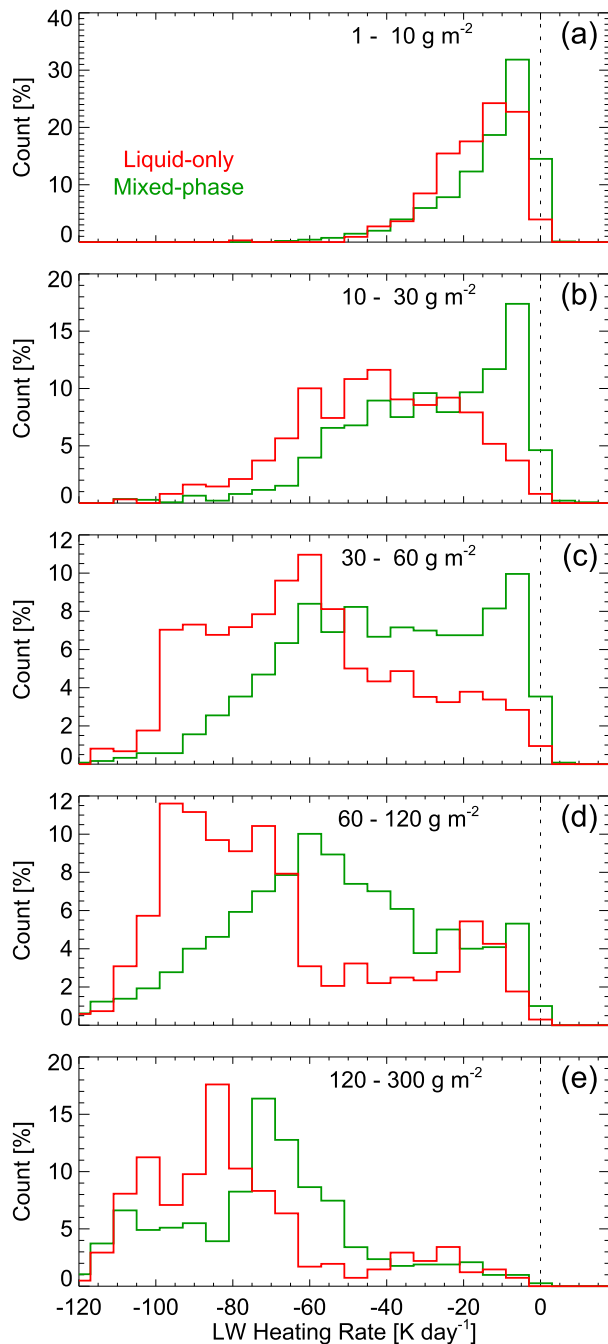


FIG. 8. Distribution of the LW RHR at the top of single-layer liquid-only (red) and mixed-phase (green) clouds for different LWP bins: (a) 1–10, (b) 10–30, (c) 30–60, (d) 60–120, and (e) 120–300 g m^{-2} . The number of cases in each LWP bin is given in Table 2.

be absorbed and thus increasing the SW RHR. Unfortunately, because of the relatively small number of cases in our dataset, further reducing the data shown in Fig. 10 into subsets by SZA or surface albedo results in relatively few cases in many LWP bins, and the median SW RHR profiles are noisy and thus they are not shown.

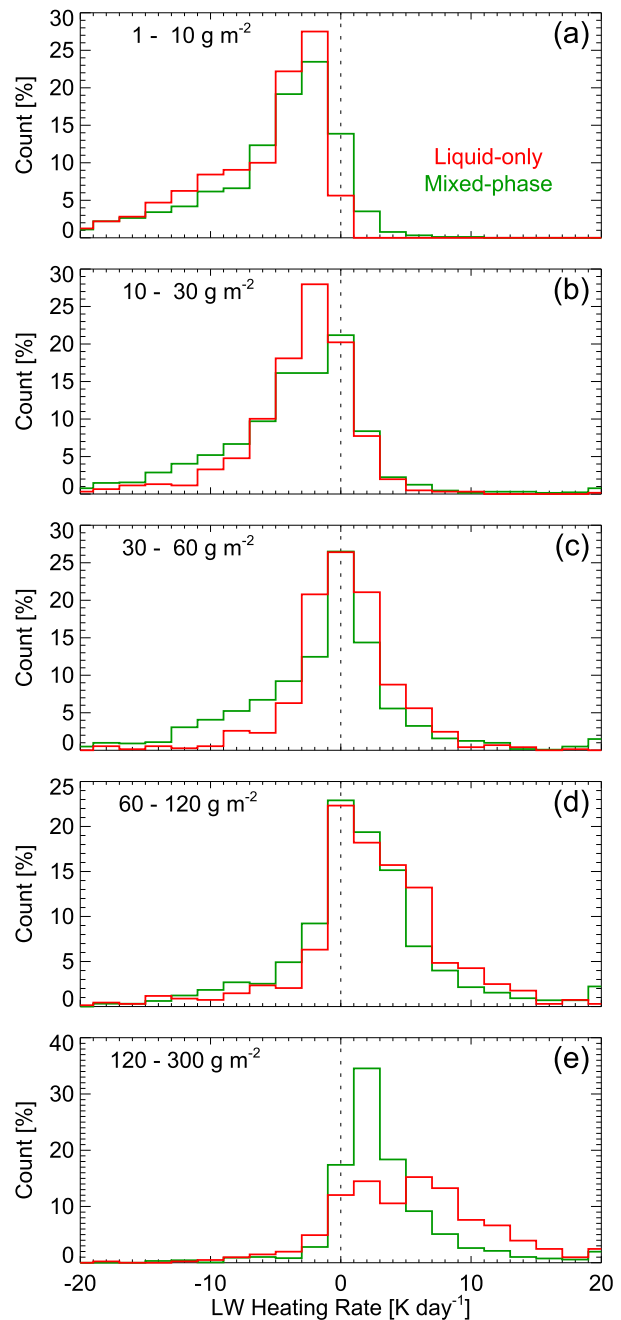


FIG. 9. As in Fig. 8, but for the base of the single-layer liquid-bearing cloud.

g. Characteristic double-layer cloud LW RHR profiles

While single-layer clouds and clear skies are the most dominant conditions at Barrow during these two years (section 3b), double-layer clouds (i.e., where two cloud layers were considered separate if there were at least two radar bins that were free of hydrometeors) were the third most common situation, occurring approximately

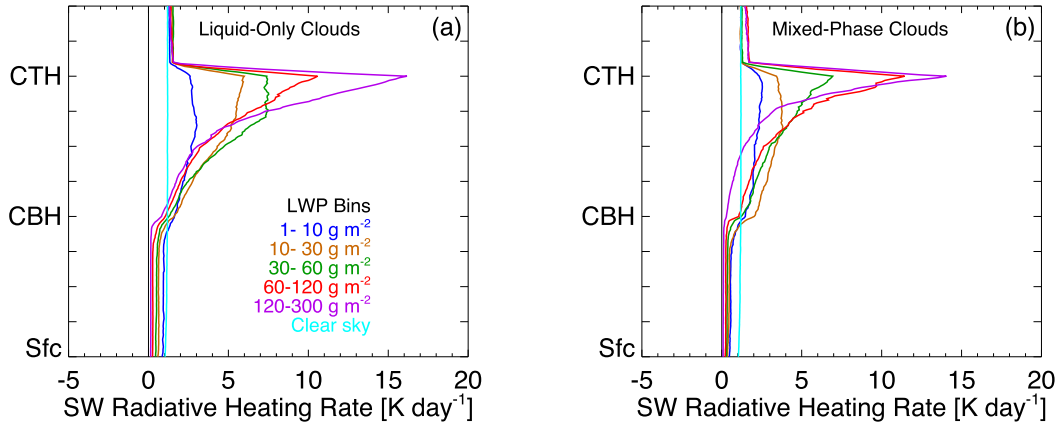


FIG. 10. The normalized vertical distribution of the median SW RHR for single-layer liquid-bearing clouds when the SZA $< 75^\circ$ using the LWP bins specified in Table 2 between Sfc, CBH, and CTH. The median clear-sky SW RHR profiles are also shown. The number of cases in each bin is shown in Table 2.

22% of the time. (Note that changing the number of hydrometeor bins used to distinguish two-layer clouds from two to three or four does not affect the results shown below significantly.) How does the presence of the second cloud layer affect the LW radiative heating profile? Many other studies have shown the sensitivity of the RHR profile to cloud overlap (e.g., L'Ecuyer et al. 2008; Chen et al. 2000b). Clearly, the addition of a second cloud layer adds considerable additional complexity to the analysis relative to single-layer clouds; this section aims to provide some initial insight into the characteristic RHR profiles for a couple different classifications given the relatively limited 2-yr dataset.

As was seen in sections 3d and 3e, the presence of liquid water greatly enhances the RHR of the cloud layer relative to a cloud that consists only of ice particles. Thus, the double-layer cloud cases were split into two categories to investigate the impact of the presence of ice and/or liquid in the different layers. The first subcategory is where both cloud layers were liquid-bearing (i.e., either liquid only or mixed phase), while the second subcategory is where the lower layer was liquid-bearing and the upper layer was ice only. The number of cases is approximately equal in both subcategories. Other possible combinations of phase for the two layers had significantly fewer samples (e.g., liquid only under liquid only, ice only under liquid bearing), and thus are not shown because of relatively poor statistics.

The characteristic LW RHR profiles for the first subcategory (i.e., liquid-bearing under liquid-bearing clouds) depends strongly on the amount of LWP in the cloud in each layer. In Fig. 11a, the RHR profile is binned by the amount of LWP in the lower cloud. Note that, just as in Fig. 7, that the RHR becomes more

negative at the top of the lower cloud as the LWP increases. However, the magnitude of the cooling at the top of this lower cloud is much smaller than in the single-layer liquid-bearing cloud (either liquid only in Fig. 7a or mixed phase in Fig. 7c) because of the radiative impact of the upper-level cloud. This demonstrates a radiative shielding of the lower layer by the upper layer (e.g., Shupe et al. 2013a). Additionally, for most of the vertical extent of the lower cloud, the cloud is actually radiatively warming the cloud layer and the atmosphere below (relative to the clear-sky RHR profile). However, as there is no correlation between the LWP in the lower and upper cloud (Table 4), there is no obvious pattern to the magnitude of the RHR in the upper cloud for when the data are sorted by the LWP in the lower cloud.

However, if we sort the LW RHR profiles by the LWP in the upper layer (Fig. 11b), several features become apparent. First, the vertical distribution of the RHR in the upper cloud is very similar to the distribution of the RHR in the single-layer liquid-bearing clouds (Figs. 7a,c). However, the peak radiative cooling at the top of the upper layer in these two-layer cloud systems is larger in magnitude with cooling rates approaching 100 K day^{-1} for cases in which the LWP in the upper layer is in the $120\text{--}300 \text{ g m}^{-2}$ subcategory (as opposed to $\sim 80 \text{ K day}^{-1}$ in the single-layer clouds); this is likely due to the reduced amount of water vapor above the top of the two-layer cloud system (relative to the single-layer cloud cases) that results in more efficient cooling to space. Also note that the radiative warming (relative to clear skies) in the middle-to-lower part of the upper-level cloud (Fig. 11b) is very similar to the radiative warming seen in the single-layer cloud systems (Figs. 7a,c). Second, there is also an apparent sorting of the magnitude of the RHR profiles in the lower cloud also, with cases

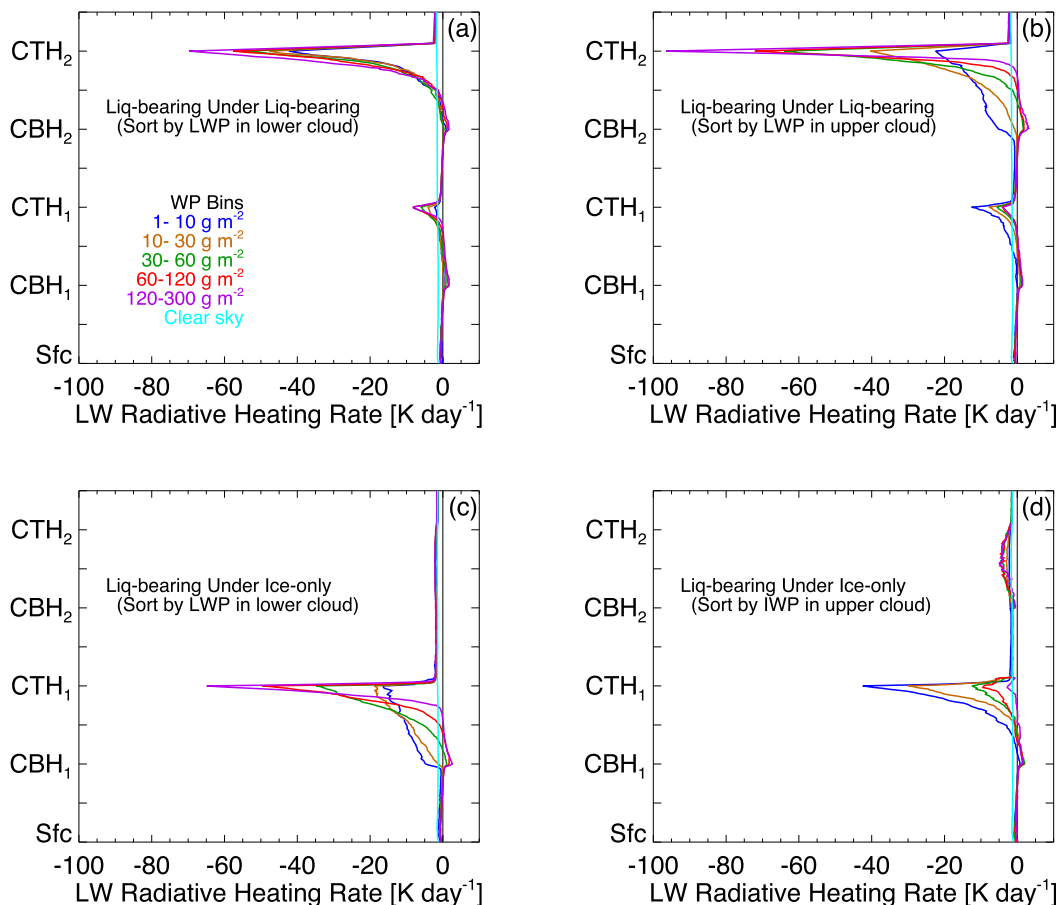


FIG. 11. The normalized vertical distribution of the median LW RHR for two-layer clouds (a),(b) where both layers contain some liquid water, or (c),(d) where only the bottom layer contains liquid water and the upper layer is ice only. The profiles were normalized between Sfc, first cloud base (CBH_1), first cloud top (CTH_1), second cloud base (CBH_2), and second cloud top (CTH_2). The data in (a) and (c) were binned according to the LWP in the lower cloud layer using the same bins as Fig. 7. In (b), the data were binned according to the LWP in the upper cloud. In (d), the data were binned by the IWP in the upper cloud using the same bin ranges.

having less LWP in the upper cloud having larger magnitude RHR in the lower cloud. This is primarily due to the reduced opacity of the upper-level cloud when its LWP is small, resulting in a larger radiative cooling at the top of the lower-level cloud; naturally, this cooling at the top of the lower-level cloud decreases as the upper-level cloud becomes more opaque and hence the radiation emitted from the upper cloud increases.

The characteristic RHR profiles for double-layer clouds where the lower level is liquid bearing and the upper layer is ice only, where the profiles are binned by the LWP in the lower-level cloud (Fig. 11c), are very similar in vertical shape and magnitude as the single-layer mixed-phase clouds (Fig. 7c). The upper-layer ice-only cloud has no apparent effect on the RHR profile of the lower cloud. Sorting the RHR profiles by the LWP

in the lower cloud also suggests that there is no radiative impact in the upper-level ice-only cloud either (Fig. 7c).

However, the correlation between the LWP in the lower cloud and the IWP in the upper cloud is essentially zero (Table 5). Furthermore, the IWP is typically at least an order of magnitude smaller than the LWP above Barrow, which results in much smaller optical depths and thereby a smaller radiative impact on the lower-level cloud. Nonetheless, if we sort the LW RHR profiles into bins associated with the IWP of the upper-level cloud (Fig. 11d), we see a slightly different picture. First, the profiles of LW RHR in the upper-level cloud are almost identical to those in the single-layer ice-only cloud (Fig. 6). Second, we again see the largest magnitude RHR in the lower cloud associated with clouds with the smallest IWP in the upper-level cloud; for example, the subcategory with IWP less than 10 g m^{-2} has a larger

TABLE 4. Statistics for two-layer cloud conditions where both layers contain liquid water. The data are binned by the amount of LWP in the lower layer, and include the ratio of LWP in the top cloud to the LWP in the bottom cloud, the correlation of the LWP between the two layers for cases in that LWP bin, and the number of cases in each bin.

LWP bin range (g m^{-2})	LWP_up/ LWP_low	Correlation	No. cases
1–10	4.60	0.03	1019
10–30	1.63	0.03	1740
30–60	0.73	0.02	957
60–120	0.43	−0.01	833
120–300	0.19	−0.28	609

TABLE 5. Statistics for two-layer cloud conditions where the lower layer contains liquid water and the top layer is ice only. The data are binned by the amount of LWP in the lower layer, and include the ratio of IWP in the top cloud to the LWP in the bottom cloud, the correlation of the LWP and IWP for the two layers for cases in that LWP bin, and the number of cases in each bin.

LWP bin range (g m^{-2})	IWP_up/ LWP_low	Correlation	No. cases
1–10	0.24	0.03	688
10–30	0.10	0.01	2702
30–60	0.02	0.01	1809
60–120	0.01	−0.07	1460
120–300	0.01	−0.03	1022

cooling rate at the top of the lower-level cloud than the subcategories with larger IWP in the upper level. This feature seen in Fig. 11d has the same explanation as that for Fig. 11b, except that since the optical depth of the upper-level cloud is less for ice-only clouds relative to liquid-bearing clouds, the lower-level cloud radiates to space more efficiently and hence has a larger LW radiative cooling rate.

4. Conclusions

This study computed the RHR profiles from a 2-yr dataset of cloud microphysical properties retrieved from ground-based remote sensors at the ARM NSA site near Barrow, Alaska. Annual composites of the SW and LW radiative heating rate profiles demonstrate large month-to-month variability, which can be explained by the seasonal dependence of the solar elevation angle and the seasonal variability of the vertical distribution of liquid and ice water contents.

From this dataset, characteristic LW and SW RHR profiles were derived for single-layer liquid-only, mixed-phase, and ice-only cloud systems. Additionally, LW RHR profiles were also computed for double-layer cloud systems; there were not enough cases to derive meaningful SW RHR statistics in these double-layer cases. These characteristic RHR profiles depend strongly on the amount and location of the liquid water. Significant differences in the vertical distribution of the RHR were seen between single-layer liquid-only clouds and single-layer mixed-phase clouds, with the former typically having larger cooling rates at cloud top. This finding is primarily due to the difference in the LWC profiles, as single-layer liquid-only clouds are typically geometrically thinner with larger LWC values than single-layer mixed-phase clouds leading to stronger cooling over a narrower layer.

As with any measurement, there are uncertainties in the derived profiles of RHR. The errors in the RHR profile depend on many factors including the accuracy of

1) the macrophysical cloud properties such as cloud height and cloud fraction; 2) the microphysical cloud properties such as IWC, LWC, and effective cloud particle size; 3) the atmospheric state such as the water vapor and temperature profiles; and 4) the radiative transfer model used to perform the calculations, which includes both the spectroscopy of the model, the scattering properties of the cloud particles, simplifications to the radiative transfer (e.g., using a 1D scattering code versus a full 3D scattering code), and more. Of all of these items, many authors have shown that the uncertainty in cloud fraction with height (which is also called “cloud overlap”) provides the largest contribution to the uncertainty in the RHR calculation (e.g., Comstock et al. 2013; Thorsen et al. 2013; Chen et al. 2000b). The uncertainties associated with the cloud properties do impact the computed RHR profiles, with uncertainties in the effective particle size having a relatively large impact on SW RHR profiles and uncertainties in the vertical distribution of cloud optical depth having the largest impact on LW RHR profiles (Comstock et al. 2013). Generally the impact of cloud property uncertainties on the RHR profile is less than 2 K day^{-1} in either the LW or SW. Thus, the uncertainties in the RHR profiles shown here that are associated with our cloud microphysics retrieval algorithm, provided that the cloud fraction is correct, is much smaller than the differences between the characteristic RHR profiles we have shown for different classifications of clouds (e.g., single-layer liquid only versus single-layer mixed phase).

There are several important messages that come from this study. Many of these messages have been illustrated in other studies (e.g., Mather et al. 2007; Haynes et al. 2013; Oreopoulos et al. 2016); however, this study demonstrates key points that are specific to Arctic clouds. One is the importance of cloud phase: a single-layer cloud containing liquid water will have RHR values at cloud top (for both LW and SW) that are

10–20 times as large as those for ice-only clouds that have the same amount of condensed water path. Second, larger amounts of water path lead to a sharper RHR gradient at cloud top in both LW and SW, and change the vertical profile shape of the RHR inside the cloud. Third, the LW radiative cooling at the top of single-layer liquid-bearing clouds is typically much larger than the SW radiative heating (if the sun is above the horizon) at the same level, resulting in overall cooling at cloud top. Fourth, for single-layer, liquid-containing clouds with LWP values above 10 gm^{-2} , the LW RHR near the bottom of the cloud is larger than clear-sky LW RHR, and the SW RHR at the same levels is larger than the clear-sky SW RHR; when combined, this results in radiative heating of the cloud base. Last, multiple cloud layers, especially when both layers contain liquid water, greatly modify the LW RHR in the lower cloud layer because of the additional downwelling LW radiation being emitted by the upper cloud; which results in radiative warming between the cloud layers (relative to the clear-sky LW RHR). Taken together, all of these radiative contributions to the diabatic heating profile below, within, and above the clouds will impact the stability of the atmosphere, driving dynamic motions within and around the cloud layers themselves. This radiatively driven instability in Arctic cloud layers is considered critically important to maintain stratiform clouds (e.g., Morrison et al. 2012; Solomon et al. 2017), which has been very difficult to achieve in numerical models at any resolution (e.g., Klein et al. 2009; Cesana et al. 2012; Solomon et al. 2017).

This study quantifies Chen et al.'s (2000b) finding that the radiative heating of clouds is very sensitive to the phase of the cloud and how clouds overlap, providing clear examples based on observations of how the RHR profile above Barrow is dependent on cloud phase and LWP. These characteristic RHR profiles can be used to evaluate how well numerical weather prediction and climate models represent Arctic clouds and their radiative impact, especially since many of these models use bulk single-moment physical parameterizations and thus must estimate effective radius in some manner (McFarlane et al. 2007).

While this study documented the impact on the RHR profiles by clouds above Barrow Alaska, it is unknown if these characteristic RHR profiles are representative of clouds throughout the Arctic. For example, RHR profiles derived from ground-based remote sensors at one tropical location were shown to agree with those from a second tropical location, after appropriately weighting each RHR profile by the relative frequency of each cloud type at the second location (Mather and McFarlane 2009). This concept needs to be evaluated

for Arctic clouds, and future work will derive similar RHR profiles at other ground-based remote sensing sites such as SHEBA in the Arctic Ocean (Uttal et al. 2002), Eureka, Canada (Cox et al. 2012), and Summit, Greenland (Shupe et al. 2013b), ideally using satellite observations to provide information on cloud fraction (e.g., Cesana et al. 2012; Kay et al. 2016), thereby allowing this hypothesis to be tested.

Acknowledgments. All datasets used in this study were obtained online from the U.S. Department of Energy (DOE) Atmospheric Radiation Measurement program (<http://www.archive.arm.gov>). This work was supported by the DOE Atmospheric System Research (ASR) program via Grants DE-SC0008830 and DE-SC0011918. We thank Eli Mlawer, Tim Shippert, Sally McFarlane, and Jim Mather for helpful discussions regarding this work. The comments and suggestions from the three anonymous reviewers improved the clarity of this manuscript and are greatly appreciated.

REFERENCES

- Asano, S., A. Uchiyama, Y. Mano, M. Murakami, and Y. Takayama, 2000: No evidence for solar absorption anomaly by marine water clouds through collocated aircraft radiation measurements. *J. Geophys. Res.*, **105**, 14 761–14 775, <https://doi.org/10.1029/2000JD900062>.
- Brenguier, J.-L., H. Pawlowska, L. Schüller, R. Preusker, J. Fisher, and Y. Fouquart, 2000: Radiative properties of boundary layer clouds: Droplet effective radius versus number concentration. *J. Atmos. Sci.*, **57**, 803–821, [https://doi.org/10.1175/1520-0469\(2000\)057<0803:RPOBLC>2.0.CO;2](https://doi.org/10.1175/1520-0469(2000)057<0803:RPOBLC>2.0.CO;2).
- Cesana, G., and T. Storelvmo, 2017: Improving climate projections by understanding how cloud phase affects radiation. *J. Geophys. Res. Atmos.*, **122**, 4594–4599, <https://doi.org/10.1002/2017JD026927>.
- , J. E. Kay, H. Chepfer, J. M. English, and G. deBoer, 2012: Ubiquitous low-level liquid-containing Arctic clouds: New observations and climate model constraints from CALIPSO-GOCCP. *Geophys. Res. Lett.*, **39**, L20804, <https://doi.org/10.1029/2012GL053385>.
- Chen, T., W. B. Rossow, and Y. Zhang, 2000a: Radiative effects of cloud-type variations. *J. Climate*, **13**, 264–286, [https://doi.org/10.1175/1520-0442\(2000\)013<0264:REOCTV>2.0.CO;2](https://doi.org/10.1175/1520-0442(2000)013<0264:REOCTV>2.0.CO;2).
- , Y. Zhang, and W. B. Rossow, 2000b: Sensitivity of atmospheric radiative heating rate profiles to variations of cloud layer overlap. *J. Climate*, **13**, 2941–2959, [https://doi.org/10.1175/1520-0442\(2000\)013<2941:SOARHR>2.0.CO;2](https://doi.org/10.1175/1520-0442(2000)013<2941:SOARHR>2.0.CO;2).
- Comstock, J. M., A. Protat, S. A. McFarlane, J. Delanoë, and M. Deng, 2013: Assessment of uncertainty in cloud radiative effects and heating rates through retrieval algorithm differences: Analysis using 3 years of ARM data at Darwin, Australia. *J. Geophys. Res. Atmos.*, **118**, 4549–4571, <https://doi.org/10.1002/jgrd.50404>.
- Cox, C. J., V. P. Walden, and P. M. Rowe, 2012: A comparison of atmospheric conditions at Eureka, Canada, and Barrow, Alaska (2006–2008). *J. Geophys. Res.*, **117**, D12204, <https://doi.org/10.1029/2011JD017164>.

- Curry, J. A., W. B. Rossow, D. Randall, and J. L. Schramm, 1996: Overview of Arctic cloud and radiation characteristics. *J. Climate*, **9**, 1731–1764, [https://doi.org/10.1175/1520-0442\(1996\)009<1731:OOACAR>2.0.CO;2](https://doi.org/10.1175/1520-0442(1996)009<1731:OOACAR>2.0.CO;2).
- Ebell, K., S. Crewell, U. Löhnert, D. D. Turner, and E. O'Connor, 2011: Cloud statistics and cloud radiative effect for a low-mountain site. *Quart. J. Roy. Meteor. Soc.*, **137**, 306–324, <https://doi.org/10.1002/qj.748>.
- Francis, P. N., J. P. Taylor, P. Hignett, and A. Slingo, 1997: On the question of enhanced absorption of solar radiation by clouds. *Quart. J. Roy. Meteor. Soc.*, **123**, 419–434, <https://doi.org/10.1002/qj.49712353809>.
- Hantel, M., and H.-R. Baader, 1978: Diabatic heating climatology of the zonal atmosphere. *J. Atmos. Sci.*, **35**, 1180–1189, [https://doi.org/10.1175/1520-0469\(1978\)035<1180:DHCOTZ>2.0.CO;2](https://doi.org/10.1175/1520-0469(1978)035<1180:DHCOTZ>2.0.CO;2).
- Haynes, J. M., T. H. Vonder Haar, T. L'Ecuyer, and D. Hendersen, 2013: Radiative heating characteristics of Earth's cloudy atmosphere from vertically resolved active sensors. *Geophys. Res. Lett.*, **40**, 624–630, <https://doi.org/10.1002/grl.50145>.
- Iacono, M. J., J. S. Delamere, E. J. Mlawer, M. W. Shephard, S. A. Clough, and W. D. Collins, 2008: Radiative forcing by long-lived greenhouse gases: Calculations with the AER radiative transfer models. *J. Geophys. Res.*, **113**, D13103, <https://doi.org/10.1029/2008JD009944>.
- Jensen, M. P., T. P. Ackerman, and S. M. Sekelsky, 2002: Radiative impacts of anvil cloud during the Maritime Continental Thunderstorm Experiment. *J. Appl. Meteor.*, **41**, 473–487, [https://doi.org/10.1175/1520-0450\(2002\)041<0473:RIOACD>2.0.CO;2](https://doi.org/10.1175/1520-0450(2002)041<0473:RIOACD>2.0.CO;2).
- Johansson, E., A. Devasthale, T. L'Ecuyer, A. M. L. Ekman, and M. Tjernström, 2015: The vertical structure of cloud radiative heating over the Indian subcontinent during summer monsoon. *Atmos. Chem. Phys.*, **15**, 11 557–11 570, <https://doi.org/10.5194/acp-15-11557-2015>.
- Kay, J. E., T. L'Ecuyer, H. Chepfer, N. Loeb, A. Morrison, and G. Cesana, 2016: Recent advances in Arctic cloud and climate research. *Curr. Climate Change Rep.*, **2**, 159, <https://doi.org/10.1007/s40641-016-0051-9>.
- Key, J. R., and J. M. Intrieri, 2000: Cloud particle phase determination with the AVHRR. *J. Appl. Meteor.*, **39**, 1797–1804, <https://doi.org/10.1175/1520-0450-39.10.1797>.
- Klein, S. A., and Coauthors, 2009: Intercomparison of model simulations of mixed-phase clouds observed during the ARM Mixed-Phase Arctic Cloud Experiment. I: Single-layered cloud. *Quart. J. Roy. Meteor. Soc.*, **135**, <https://doi.org/10.1002/qj.416>.
- Kollias, P., and Coauthors, 2016: Development and applications of ARM millimeter-wavelength cloud radars. *The Atmospheric Radiation Measurement (ARM) Program: The First 20 Years, Meteor. Monogr.*, No. 57, Amer. Meteor. Soc., 17.1–17.19, <https://doi.org/10.1175/AMSMONOGRAPHIS-D-15-0037.1>.
- L'Ecuyer, T. S., N. B. Wood, T. Haladay, G. L. Stephens, and P. W. Stackhouse Jr., 2008: Impact of clouds on atmospheric heating based on the R04 CloudSat fluxes and heating rates data set. *J. Geophys. Res.*, **113**, D00A15, <https://doi.org/10.1029/2008JD009951>.
- Mace, G. G., S. Benson, and S. Kato, 2006: Cloud radiative forcing at the Atmospheric Radiation Measurement program climate research facility: 2. Vertical redistribution of radiant energy by clouds. *J. Geophys. Res.*, **111**, D11S91, <https://doi.org/10.1029/2005JD005922>.
- Mather, J. H., and S. A. McFarlane, 2009: Cloud classes and radiative heating profiles at the Manus and Nauru Atmospheric Radiation Measurement (ARM) sites. *J. Geophys. Res.*, **114**, D19204, <https://doi.org/10.1029/2009JD011703>.
- , —, M. A. Miller, and K. L. Johnson, 2007: Cloud properties and associated radiative heating rates in the tropical western Pacific. *J. Geophys. Res.*, **112**, D05201, <https://doi.org/10.1029/2006JD007555>.
- McClatchey, R. A., R. W. Fenn, J. A. A. Selby, F. E. Volz, and J. S. Garing, 1970: Optical properties of the atmosphere. AFCRL TR70-0527, AD715270, 113 pp.
- McFarlane, S. A., J. H. Mather, and T. P. Ackerman, 2007: Analysis of tropical radiative heating profiles: A comparison of models and observations. *J. Geophys. Res.*, **112**, D14218, <https://doi.org/10.1029/2006JD008290>.
- , —, and E. J. Mlawer, 2016: ARM's progress on improving atmospheric broadband radiative fluxes and heating rates. *The Atmospheric Radiation Measurement (ARM) Program: The First 20 Years, Meteor. Monogr.*, No. 57, Amer. Meteor. Soc., 20.1–20.24, <https://doi.org/10.1175/AMSMONOGRAPHIS-D-15-0046.1>.
- Mlawer, E. J., S. J. Traubman, P. D. Brown, M. J. Iacono, and S. A. Clough, 1997: RRTM, a validated correlated-*k* model for the longwave. *J. Geophys. Res.*, **102**, 16 663–16 682, <https://doi.org/10.1029/97JD00237>.
- , M. J. Iacono, R. Pincus, H. W. Barker, L. Oreopoulos, and D. L. Mitchell, 2016: Contributions of the ARM program to radiative transfer modeling for climate and weather applications. *The Atmospheric Radiation Measurement (ARM) Program: The First 20 Years, Meteor. Monogr.*, No. 57, Amer. Meteor. Soc., 15.1–15.19, <https://doi.org/10.1175/AMSMONOGRAPHIS-D-15-0041.1>.
- Morrison, H., G. de Boer, G. Feingold, J. Harrington, M. D. Shupe, and K. Sulia, 2012: Resilience of persistent Arctic mixed-phase clouds. *Nat. Geosci.*, **5**, 11–17, <https://doi.org/10.1038/ngeo1332>.
- Oreopoulos, L., N. Cho, D. Lee, and S. Kato, 2016: Radiative effects of global MODIS cloud regimes. *J. Geophys. Res. Atmos.*, **121**, 2299–2317, <https://doi.org/10.1002/2015JD024502>.
- Protat, A., and Coauthors, 2014: Reconciling ground-based and space-based estimates of the frequency of occurrence and radiative effect of clouds around Darwin, Australia. *J. Appl. Meteor. Climatol.*, **53**, 456–478, <https://doi.org/10.1175/JAMC-D-13-072.1>.
- Settle, J. J., N. A. Bharmal, G. J. Robinson, and A. Slingo, 2008: Sampling uncertainties in surface radiation budget calculations in RADAGAST. *J. Geophys. Res.*, **113**, D00E02, <https://doi.org/10.1029/2008JD010509>.
- Shupe, M. D., 2011: Clouds at Arctic atmospheric observatories. Part II: Thermodynamic phase characteristics. *J. Appl. Meteor. Climatol.*, **50**, 645–661, <https://doi.org/10.1175/2010JAMC2468.1>.
- , and J. M. Intrieri, 2004: Cloud radiative forcing of the Arctic surface: The influence of cloud properties, surface albedo, and solar zenith angle. *J. Climate*, **17**, 616–628, [https://doi.org/10.1175/1520-0442\(2004\)017<0616:CRFOTA>2.0.CO;2](https://doi.org/10.1175/1520-0442(2004)017<0616:CRFOTA>2.0.CO;2).
- , P. O. G. Persson, I. M. Brooks, M. Tjernström, J. Sedlar, T. Mauritsen, S. Sjogren, and C. Leck, 2013a: Cloud and boundary layer interactions over the Arctic sea-ice in late summer. *Atmos. Chem. Phys.*, **13**, 9379–9400, <https://doi.org/10.5194/acp-13-9379-2013>.
- , and Coauthors, 2013b: High and dry: New observations of tropospheric and cloud properties above the Greenland ice sheet. *Bull. Amer. Meteor. Soc.*, **94**, 169–186, <https://doi.org/10.1175/BAMS-D-11-00249.1>.

- , D. D. Turner, A. B. Zwink, M. M. Thieman, M. J. Mlawer, and T. R. Shippert, 2015: Deriving Arctic cloud microphysics at Barrow, Alaska: Algorithms, results, and radiative closure. *J. Appl. Meteor. Climatol.*, **54**, 1675–1689, <https://doi.org/10.1175/JAMC-D-15-0054.1>.
- Slingo, A., S. Nicholls, and J. Schmetz, 1982: Aircraft observations of marine stratocumulus during JASIN. *Quart. J. Roy. Meteor. Soc.*, **108**, 833–856, <https://doi.org/10.1002/qj.49710845807>.
- , H. E. White, N. A. Bharmal, and G. J. Robinson, 2009: Overview of observations from the RADAGAST experiment in Niamey, Niger: 2. Radiative fluxes and divergences. *J. Geophys. Res.*, **114**, D00E04, <https://doi.org/10.1029/2008JD010497>.
- Sohn, B.-J., 1999: Cloud-induced infrared radiative heating and its implications for large-scale tropical circulations. *J. Atmos. Sci.*, **56**, 2657–2672, [https://doi.org/10.1175/1520-0469\(1999\)056<2657:CIIRHA>2.0.CO;2](https://doi.org/10.1175/1520-0469(1999)056<2657:CIIRHA>2.0.CO;2).
- Solomon, A., M. D. Shupe, O. Persson, H. Morrison, T. Yamaguchi, P. M. Caldwell, and G. de Boer, 2014: The sensitivity of springtime Arctic mixed-phase stratocumulus clouds to surface-layer and cloud-top inversion-layer moisture sources. *J. Atmos. Sci.*, **71**, 574–595, <https://doi.org/10.1175/JAS-D-13-0179.1>.
- , —, and N. B. Miller, 2017: Cloud–atmospheric boundary layer–surface interactions on the Greenland Ice Sheet during the July 2012 extreme melt event. *J. Climate*, **30**, 3237–3252, <https://doi.org/10.1175/JCLI-D-16-0071.1>.
- Stamnes, K., R. G. Ellingson, J. A. Curry, J. E. Walsh, and B. D. Zak, 1999: Review of science issues, deployment strategy, and status for the ARM North Slope of Alaska–Adjacent Arctic Ocean climate research site. *J. Climate*, **12**, 46–63, <https://doi.org/10.1175/1520-0442-12.1.46>.
- Stephens, G. L., 1978: Radiation profiles in extended water clouds. II: Parameterization schemes. *J. Atmos. Sci.*, **35**, 2123–2132, [https://doi.org/10.1175/1520-0469\(1978\)035<2123:RPIEWC>2.0.CO;2](https://doi.org/10.1175/1520-0469(1978)035<2123:RPIEWC>2.0.CO;2).
- , 2005: Cloud feedbacks in a climate system: A critical review. *J. Climate*, **18**, 237–273, <https://doi.org/10.1175/JCLI-3243.1>.
- Thorsen, T. J., Q. Fu, and J. M. Comstock, 2013: Cloud effects on radiative heating rate profiles over Darwin using ARM and A-train radar/lidar observations. *J. Geophys. Res. Atmos.*, **118**, 5637–5654, <https://doi.org/10.1002/jgrd.50476>.
- Turner, D. D., S. A. Clough, J. C. Liljegren, E. E. Clothiaux, K. Cady-Pereira, and K. L. Gaustad, 2007: Retrieving liquid water path and precipitable water vapor from Atmospheric Radiation Measurement (ARM) microwave radiometers. *IEEE Trans. Geosci. Remote Sens.*, **45**, 3680–3690, <https://doi.org/10.1109/TGRS.2007.903703>.
- Uttal, T., and Coauthors, 2002: Surface Heat Budget of the Arctic Ocean. *Bull. Amer. Meteor. Soc.*, **83**, 255–275, [https://doi.org/10.1175/1520-0477\(2002\)083<0255:SHBOTA>2.3.CO;2](https://doi.org/10.1175/1520-0477(2002)083<0255:SHBOTA>2.3.CO;2).
- Valero, F. P. J., R. D. Cess, M. Zhang, S. K. Pope, A. Bucholtz, B. Bush, and J. Vitko, 1997: Absorption of solar radiation by the cloudy atmosphere: Interpretations of collocated aircraft measurements. *J. Geophys. Res.*, **102**, 29 917–29 927, <https://doi.org/10.1029/97JD01782>.
- Verlinde, J., B. D. Zak, M. D. Shupe, M. D. Ivey, and K. Stamnes, 2016: The ARM North Slope of Alaska (NSA) sites. *The Atmospheric Radiation Measurement (ARM) Program: The First 20 Years, Meteor. Monogr.*, No. 57, Amer. Meteor. Soc., 8.1–8.13, <https://doi.org/10.1175/AMSMONOGRAPHS-D-15-0023.1>.
- Wood, R., 2012: Stratocumulus clouds. *Mon. Wea. Rev.*, **140**, 2373–2423, <https://doi.org/10.1175/MWR-D-11-00121.1>.
- Zender, C. S., B. Bush, S. K. Pope, A. Bucholtz, W. D. Collins, J. T. Kiehl, F. P. J. Valero, and J. Vitko, 1997: Atmospheric absorption during the Atmospheric Radiation Measurement (ARM) Enhanced Shortwave Experiment (ARESE). *J. Geophys. Res.*, **102**, 29 901–29 915, <https://doi.org/10.1029/97JD01781>.